J. Phys. B: At. Mol. Opt. Phys. **30** (1997) 3543–3565. Printed in the UK PII: S0953-4075(97)82237-7

Electron-impact excitation and ionization of Ar^+ for the determination of impurity influx in tokamaks

D C Griffin†, M S Pindzola‡, J A Shaw‡, N R Badnell§, M O'Mullane‖ and H P Summers§

† Department of Physics, Rollins College, Winter Park, FL 32789, USA
‡ Department of Physics, Auburn University, Auburn, AL 36849, USA
§ Department of Physics and Applied Physics, University of Strathclyde, Glasgow G4 0NG, UK
‖ JET Joint Undertaking, Abingdon, Oxon, OX14 3EA, UK

Received 3 March 1997

Abstract. Electron-impact excitation for Ar^+ is studied using close-coupling R-matrix theory in LS coupling. Both 28-state and 40-state close-coupling approximations are employed and cross sections and effective collision strengths for selected excitation transitions are compared. In addition, ionization rate coefficients for Ar^+ are determined using distorted-wave theory and compared with experiment. Finally, these data, along with experimental and theoretical radiative rates, are entered into a collisional-radiative modelling program–(atomic data and analysis structure) to obtain SXB ratios for the radiative transitions $3p^4(^3P)4p\,^4D \rightarrow 3p^4(^3P)4s\,^4P$ and $3p^4(^3P)4p\,^2D \rightarrow 3p^4(^3P)4s\,^2P$. These SXB ratios allow one to relate spectroscopic emissivity measurements to impurity influx from a localized source. In the present studies, we modelled the impurity influx when only the ground term contributes to the ionization of Ar^+ and showed that the SXB ratio corresponding to the radiative transition between the doublet terms is less sensitive to electron density and more reliable than the SXB ratio corresponding to the radiative transition between the quartet terms. Additional collisional–radiative modelling studies of impurity influx when the ground and metastable states contribute to the ionization of Ar^+ are also proposed.

1. Introduction

Currently there is significant interest in inelastic scattering of electrons from complex atoms and low-charge-state ions. This is primarily due to the need for accurate atomic data for application to studies of magnetically confined plasmas near the walls of fusion reactors and to low-temperature astrophysical plasmas. One of the elements of present interest to experimental studies in tokamak reactors is argon. For example, at JET argon gas is puffed into the divertor both in order to detach the plasma from the divertor plates and to radiatively cool it (Horton 1996), while at Alcator C-Mod at MIT the recycling of argon from the divertor surface is being studied (McCracken 1996).

It is possible to relate spectroscopic measurements of emissivities along a line of sight directed towards a localized source of impurities to the impurity flux from that source by employing theoretical calculations of the number of ionizations per emitted photon (Behringer *et al* 1989, Badnell *et al* 1996). Data for any particular ionization stage of the atomic species of interest can be employed as long as no higher ionization stages of that atom emerge from the localized source. Thus, such spectroscopic measurements for certain radiative transitions in Ar^+, in combination with radiative rates, electron-impact excitation

0953-4075/97/153543+23$19.50

rates, and electron-impact ionization rates for that ion would allow for the determination of the influx of argon.

In the low-density limit, the number of ionizations per emitted photon can be determined simply from the ionization rate from the ground state divided by the excitation rate from the ground state to the upper level of the observed spectral line times the radiative branching ratio for that observed line; this is the zero-density SXB ratio. However, one must still correct the excitation rate for the effects of radiative cascades from higher-lying levels. In addition, we will show that for certain types of transitions, even in the absence of cascades, the zero-density SXB ratio may differ significantly from the density-dependent SXB ratio even at quite low electron densities. Thus, in order to employ SXB ratios for the determination of impurity influx, one must normally include the effects of collisions on the populations of the excited states; this is especially true for the higher densities present in the divertor region of a tokamak plasma. The atomic level populations can be determined by using a collisional–radiative model (see for example, Summers and Hooper 1983).

Recently, Tayal and Henry (1996) reported on LS-coupling R-matrix calculations of electron-impact excitation collision strengths from the ground term of Ar^+ to various doublet excited terms. They employed both nine-state and 19-state approximations, but included only doublet terms in their close-coupling (CC) expansions. In the present study, we focus on excitation from the $3p^5\,{}^2P$ ground term to the $3p^4(^3P)4p\,{}^4D$ excited term followed by radiation to the $3p^4(^3P)4s\,{}^4P$ term and excitation from the $3p^5\,{}^2P$ ground term to the $3p^4(^3P)4p\,{}^2D$ excited term followed by radiation to the $3p^4(^3P)4s\,{}^2P$ term. However, we also need rates for collisional excitation and de-excitation between a large number of excited terms in order to determine term populations as a function of electron density. This requires a much more extensive set of excitation calculations.

In the present work, we have employed both 28-state and 40-state CC approximations to make R-matrix calculations of excitation rates between a large number of LS terms. Great care had to be taken to carry the partial-wave expansions to sufficiently high values of the total angular momentum so that the excitation cross sections from excited terms, for which the threshold energies are relatively low, were sufficiently accurate at higher energies that they could be used for the determination of the rate coefficients. In addition, we have calculated the rate coefficient for ionization from the ground term of Ar^+ using the distorted-wave (DW) approximation and compared our result with a rate determined from experimental measurements. The rate coefficients for excitation and ionization and the radiative rates were then used in the quasistatic generalized collisional–radiative level population model incorporated in the atomic data and analysis structure (ADAS), see Summers (1994), to determine SXB ratios as a function of electron density and temperature, and to calculate the power-loss coefficient as a function of temperature.

This paper is organized as follows. In section 2 we describe our atomic structure calculations, our R-matrix calculations of electron-impact excitation, and our DW calculations of electron-impact ionization. In section 3, we present a discussion of population modelling and our results for the density-dependent SXB ratios and the zero-density power-loss coefficient. In section 4 we summarize our findings and propose additional collisional–radiative modelling studies for Ar^+.

2. Atomic theory

2.1. Atomic structure

The bound-state radial wavefunctions employed in this study were determined using Fischer's multiconfiguration Hartree–Fock (MCHF) programmes (Froese Fischer 1991). The bound-state energies and radiative rates were determined from a set of configuration-interaction (CI) calculations and include the effects of the Darwin and mass–velocity terms; however, these relativistic corrections are relatively small for this ion. We employed two different CI basis sets: the first included the 28 terms arising from the configurations $3s^23p^5$, $3s3p^6$, $3s^23p^43d$, $3s^23p^44s$, and $3s^23p^44p$; the second included the above 28 terms plus the 12 terms of the configuration $3s^23p^44d$, and the three non-spectroscopic terms (pseudostates) $3s^23p^4(^3P)\bar{5}s\,^2P$, $3s^23p^4(^3P)\bar{5}p\,^2D$, and $3s^23p^4(^1D)\bar{5}p\,^2D$—a total of 43 terms. As explained below, the latter three pseudostates, that include non-spectroscopic orbitals designated by a line over the principal number specification, were included solely to improve the atomic structure.

The 1s, 2s, 2p, 3s, and 3p orbitals were determined from a single-configuration Hartree–Fock (SCHF) calculation on $3p^5\,^2P$, and these orbitals were then frozen while optimizing all other orbitals. The 4s and 4p orbitals were determined from SCHF calculations on $3p^4(^3P)4s\,^4P$ and $3p^4(^3P)4p\,^4D$, respectively. The 3d orbital was determined from a configuration-average (CA) Hartree–Fock calculation on the $3p^43d$ configuration. This CA 3d orbital should provide the best overall estimate for this orbital in all the terms of the $3p^43d$ configuration. The 4d orbital employed in the 43-state CI calculation was determined by performing an SCHF calculation on $3p^4(^3P)4d\,^4D$. This provides a good estimate for the 4d orbital in the lower-lying quartet terms of the $3p^44d$ configuration; in addition, through CI between the quartet terms of $3p^43d$ and $3p^44d$, it allows us to better correct the CA 3d orbital in the important quartet terms of the $3p^43d$ configuration for LS term dependence. The $\bar{5}s$ pseudo-orbital was determined from an MCHF calculation on $3p^4(^3P)4s\,^2P$ plus $3p^4(^3P)\bar{5}s\,^2P$ to correct the 4s orbital in the ^2P term for LS term dependence. Finally, the $\bar{5}p$ pseudo-orbital was determined from an MCHF calculation on $3p^4(^3P)4p\,^2D + 3p^4(^1D)4p\,^2D + 3p^4(^3P)\bar{5}p\,^2D + 3p^4(^1D)\bar{5}p\,^2D$ to correct the 4p orbital for LS term dependence in the ^2D terms.

The energies for all of the terms from the 28-term CI calculation and the 40 spectroscopic terms from the 43-term CI calculations are given in table 1, and compared with energies used in the 19-state R-matrix CC calculation of Tayal and Henry (1996) and the experimental energies from Moore (1949). With respect to energy, only the highest four terms of $3p^43d$ ($3p^4(^3P)3d\,^2D$, $3p^4(^3P)3d\,^2P$, $3p^4(^1S)3d\,^2D$, and $3p^4(^1D)3d\,^2S$) are affected much by the extra CI included in the 43-term CI basis set, and they are all pushed down closer to the experimental values. In the case of the 43-term CI calculation, the first eight terms of $3p^44d$ are in reasonably good agreement with experiment; however, in the absence of any higher terms to compensate for CI with the lower terms, the energies of the last four terms are in poor agreement with experiment.

Although the energies of the first 36 of the 40 spectroscopic terms included in the 43-term CI calculation are in good overall agreement with experiment, some of the calculated terms are out of energy order, as compared with experiment. However, our primary interest for this study is excitations to the ^4D and ^2D terms of $3p^4(^3P)4p$. As can be seen from table 1, these two terms are in excellent agreement with experimental energies; furthermore, none of the terms that are calculated to be below these two terms are found experimentally to be above them, and none that are calculated to be above these terms are actually below

Table 1. Calculated term energies of Ar^+ in eV relative to the ground term.

Index	Term	Present 43-term CI	Present 28-term CI	TH[a] 19-state CC	Experimental[b]
1	$3p^5\,^2P$	0.00	0.00	0.00	0.00
2	$3s3p^6\,^2S$	12.85	13.18	13.44	13.48
3	$3p^4(^3P)3d\,^4D$	15.93	16.05	—	16.42
4	$3p^4(^3P)4s\,^4P$	16.73	16.73	—	16.71
5	$3p^4(^3P)3d\,^4F$	17.34	17.37	—	17.69
6	$3p^4(^3P)4s\,^2P$	17.39	17.44	18.94	17.18
7	$3p^4(^1D)3d\,^2P$	17.99	18.06	19.27	18.02
8	$3p^4(^3P)3d\,^4P$	18.13	18.12	—	18.31
9	$3p^4(^1D)3d\,^2D$	18.47	18.52	20.53	18.70
10	$3p^4(^3P)3d\,^2F$	18.54	18.56	19.95	18.54
11	$3p^4(^1D)4s\,^2D$	18.99	19.02	19.87	18.44
12	$3p^4(^1D)3d\,^2G$	19.05	19.08	—	19.12
13	$3p^4(^3P)4p\,^4P$	19.19	19.19	—	19.25
14	$3p^4(^3P)4p\,^4D$	19.54	19.54	—	19.55
15	$3p^4(^3P)4p\,^2D$	19.79	19.81	21.26	19.71
16	$3p^4(^3P)4p\,^2P$	20.05	20.05	21.34	19.85
17	$3p^4(^3P)4p\,^2S$	20.08	20.08	21.46	19.97
18	$3p^4(^3P)4p\,^4S$	20.08	20.08	—	19.97
19	$3p^4(^1D)3d\,^2F$	20.52	20.55	—	20.26
20	$3p^4(^1D)4p\,^2F$	21.40	21.40	22.95	21.14
21	$3p^4(^1S)4s\,^2S$	21.64	21.71	22.93	20.74
22	$3p^4(^1D)4p\,^2D$	21.82	21.84	22.95	21.50
23	$3p^4(^3P)3d\,^2D$	21.91	22.73	23.22	21.39
24	$3p^4(^3P)3d\,^2P$	22.10	24.33	23.36	21.64
25	$3p^4(^1D)4p\,^2P$	22.24	22.24	23.13	21.38
26	$3p^4(^3P)4d\,^4D$	22.74	—	—	22.79
27	$3p^4(^1S)3d\,^2D$	22.87	25.26	—	22.79
28	$3p^4(^3P)4d\,^4F$	22.97	—	—	23.10
29	$3p^4(^3P)4d\,^4P$	23.13	—	—	23.14
30	$3p^4(^3P)4d\,^2F$	23.26	—	—	23.20
31	$3p^4(^1D)3d\,^2S$	23.76	26.70	24.36	22.83
32	$3p^4(^1D)4d\,^2P$	24.18	—	—	23.60
33	$3p^4(^1S)4p\,^2P$	24.51	24.51	26.10	23.82
34	$3p^4(^1D)4d\,^2D$	24.72	—	—	23.88
35	$3p^4(^1D)4d\,^2G$	24.82	—	—	24.62
36	$3p^4(^1D)4d\,^2F$	25.14	—	—	24.82
37	$3p^4(^1D)4d\,^2P$	27.10	—	—	24.74
38	$3p^4(^3P)4d\,^2D$	27.28	—	—	24.77
39	$3p^4(^1S)4d\,^2D$	28.33	—	—	—
40	$3p^4(^1D)4d\,^2S$	28.46	—	27.02	25.45

[a] Tayal and Henry (1996).
[b] Moore (1949).

them. Thus, we would expect that the disagreement between the calculated and experimental energy order will have only a small effect on the resonance contribution to the excitation cross section for these two terms. However, these differences in energy order could affect the resonance contributions to excitation between other terms and thereby have some effect on the density-dependent collisional–radiative modelling of this problem.

In table 2, we present our results for the emission oscillator strengths in both the length and velocity gauges and the radiative rates in the length gauge for the dipole-

Table 2. Emission oscillator strengths and radiative rates from the $3p^4(^3P)4p\,^4D$, $3p^4(^3P)4p\,^2D$ and $3p^4(^3P)4s\,^2P$ terms of Ar^+.

		28-term CI		43-term CI		Experiment (VW)[a]
	Final term	f_L/f_V	A (10^8 s^{-1})	f_L/f_V	A(10^8 s^{-1})	A (10^8 s^{-1})
1	$3p^4(^3P)4p\,^4D$					
	$3p^4(^3P)4s\,^4P$	0.367/0.361	1.260	0.365/0.364	1.260	1.110
	$3p^4(^3P)3d\,^4D$	0.052/0.010	0.272	0.031/0.023	0.174	0.107
	$3p^4(^3P)3d\,^4F$	0.180/0.092	0.368	0.139/0.149	0.292	0.151
	$3p^4(^3P)3d\,^4P$	0.010/0.027	0.008	0.009/0.026	0.008	—
2	$3p^4(^3P)4p^2D$					
	$3p^4(^3P)4s\,^2P$	0.299/0.414	0.727	0.339/0.360	0.848	0.843
	$3p^4(^1D)3d\,^2P$	0.020/0.042	0.023	0.016/0.021	0.023	—
	$3p^4(^1D)3d\,^2D$	0.006/0.010	0.004	0.008/0.005	0.006	—
	$3p^4(^3P)3d\,^2F$	0.098/0.147	0.066	0.084/0.180	0.057	—
3	$3p^4(^3P)4s\,^2P$					
	$3p^5\,^2P$	0.243/0.238	32.1	0.226/0.206	29.6	—

[a] Vujnović and Wiese (1992)

allowed transitions from the ^4D and ^2D terms of $3p^4(^3P)4p$. The average wavelength for the transition between the $3p^4(^3P)4p\,^4D$ term and the $3p^4(^3P)4s\,^4P$ term is 436 nm, while that for the transition from the $3p^4(^3P)4p\,^2D$ term to the $3p^4(^3P)4s\,^2P$ term is 490 nm. Emissivity measurements of the spectral lines corresponding to these transitions should be quite appropriate for the determination of the flux of Ar within the divertor of a tokamak reactor. The improvement in agreement between length and velocity oscillator strengths and the theoretical and experimental radiative rates seen in the 43-term CI calculation for the above doublet transition is due to the correction for LS term dependence provided by the inclusion of the doublet pseudostates in the 43-term CI. We also show in this table the oscillator strengths and radiative rate for the transitions between the $3p^4(^3P)4s\,^2P$ term and the ground term. As we shall see in section 3, the radiative rate for this transition has an important effect on the collisional–radiative modelling of the doublet transition at 490 nm.

Although CI has only a small effect on the energy of the ^4D and ^4F terms of $3p^4(^3P)3d$, it is seen from table 2 to have a pronounced effect on the oscillator strengths and radiative rates for the transitions from the $3p^4(^3P)4p\,^4D$ term to the $3p^4(^3P)3d\,^4D$ and $3p^4(^3P)3d\,^4F$ terms. This is primarily due to the correction of the CA 3d orbital for LS term dependence through CI with the quartet terms of $3p^4$4d. The agreement between the length and velocity oscillator strengths is much better and the agreement between the theoretical and experimental radiative rates is closer for the 43-state CI basis set than for the 28-state basis. However, there are still significant discrepancies between our calculated radiative rates and the experimental values. We have attempted to further correct these particular radiative rates by including certain additional pseudostates in the CI expansion. However, the changes that resulted were relatively small; this indicates that a much larger CI expansion may be required to obtain further improvement, and this would significantly complicate our CC calculations of electron-impact excitation.

For our collisional–radiative modelling of Ar^+, we have employed our theoretical radiative rates for all dipole-allowed transitions, with the exception of the four transitions for which radiative rates are given in the last column of table 2; for those transitions, the experimental values were employed. In addition, we performed intermediate-coupling CI calculations to determine approximate radiative rates for the dipole-forbidden radiative

transitions from levels of the metastable terms $3p^4(^3P)3d\,^4D$, $3p^4(^3P)4s\,^4P$, $3p^4(^3P)3d\,^4F$, $3p^4(^3P)3d\,^4P$, and $3p^4(^3P)3d\,^2F$ to the $3p^5\,^2P$ ground term. However, since the levels of these terms radiate to the levels of the ground term through weak spin–orbit mixing with levels that make strong dipole transitions to the levels of $3p^5\,^2P$, these rates are very uncertain. In addition to the above five terms, the levels of $3p^4(^3P)3d\,^2G$ cannot make dipole transitions to levels of the ground term through such mixing and the radiative rate for this term was assumed to be zero in our calculations. Finally, we find that although the term listed with the label $3p^4(^1D)3d\,^2D$ in table 1 can make a dipole-allowed radiative transition to $3p^5\,^2P$, it is strongly mixed with $3p^4(^3P)3d\,^2D$ and through cancellation in the eigenvectors radiates only weakly to the ground term. Thus we have as many as seven metastable terms; as we shall see, this significantly complicates the collisional–radiative modelling of Ar^+.

2.2. Electron-impact excitation

Two *R*-matrix CC calculations of electron-impact excitation were performed. The first, that we refer to as the 28-state CC calculation, employed the 28-term CI basis set and included all 28 terms within the CC expansion, while the second, that we refer to as the 40-state CC calculation, employed the 43-state CI basis set and included the 40 spectroscopic terms within the CC expansion. In the case of the 28-state CC calculation, the radius of the *R*-matrix boundary, r_B, was 18.7 au and the number of basis orbitals, N_C, used to represent the continuum for a given value of angular momentum was 22; in the case of the 40-state CC calculation, r_B was 23.3 au and N_C was 31. It is well known that the inclusion of pseudostates in a CI basis set that are not included in the CC expansion of the target leads to the presence of pseudo resonances. In our 40-state CC calculation, these pseudo resonances were eliminated by using a transformation and reduction method explained in Gorczyca *et al* (1995).

These calculations were carried out with full exchange for all $LS\Pi$ partial waves with $2S + 1 = 1$, 3, and 5, $L = 0$–12, and both even and odd parity, using the Breit–Pauli *R*-matrix codes in the *LS* mode (see Berrington *et al* 1995). However, for excitations between excited terms, where the threshold energies are relatively low, this partial-wave expansion is not sufficiently complete to permit accurate calculations at high energies; thus, in order to obtain sufficiently accurate rate coefficients for transitions between these terms, one must include partial waves with much higher values of L. For this reason, we also performed 28- and 40-state no-exchange CC *R*-matrix calculations (see Burke *et al* 1992), from $L = 13$ to $L = 40$, and then 'topped up' these results, using the method described by Burgess (1974) for dipole-allowed transitions and by assuming that the partial collision strengths form a geometric series in L (see Burgess *et al* 1970) for quadrupole transitions. Finally, these high L contributions were added to the full-exchange *R*-matrix results.

In figures 1 and 2, we compare our 28- and 40-state CC calculations of the excitation cross sections from the $3p^5\,^2P$ ground term to the ^4D and ^2D terms of $3p^4(^3P)4p$, respectively. These are the two primary excitation transitions to be considered in this study. As can be seen, the difference between these two calculations with respect to the background contribution to the ^4D cross section is quite small. The resonance contributions from the two calculations are somewhat different but this has a small effect on the rate coefficient for this transition. The difference between these two calculations for the ^2D cross section is somewhat larger; this is not only due to the coupling of the bound terms by the continuum electron (coupling effects), but also to the correction for *LS* term dependence in $3p^4(^3P)4p\,^2D$ that is included in the 43-term CI basis set, but not the 28-term CI basis set. However, the resonance contribution to the cross section from the 40-state CC calculation

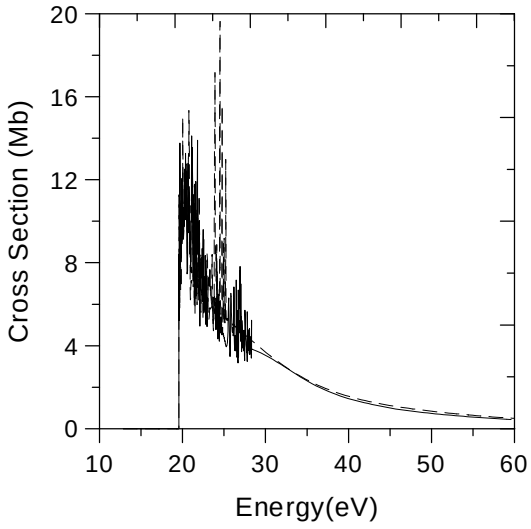

Figure 1. Electron-impact excitation cross section for the transition $3p^5\,{}^2P \rightarrow 3p^4({}^3P)4p\,{}^4D$ in Ar^+ from a 28-state *R*-matrix CC calculation (broken curve) and a 40-state *R*-matrix CC calculation (full curve).

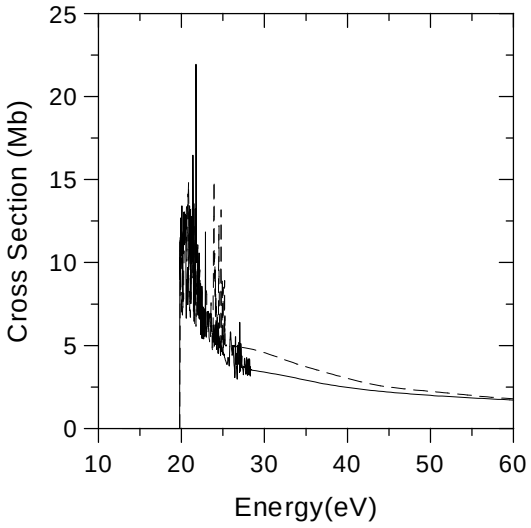

Figure 2. Electron-impact excitation cross section for the transition $3p^5\,{}^2P \rightarrow 3p^4({}^3P)4p\,{}^2D$ in Ar^+ from a 28-state *R*-matrix CC calculation (broken curve) and a 40-state *R*-matrix CC calculation (full curve).

is somewhat larger than that from the 28-state CC calculation, while the reverse is true for the background contribution; thus, the overall difference between the rate coefficients determined from these two calculations is relatively small.

In figures 3 and 4, we compare the 28- and 40-state CC cross sections for excitation from the ground term to $3p^4({}^3P)4s\,{}^4P$, and the cross section for excitation from $3p^4({}^3P)4s\,{}^4P$ to $3p^4({}^3P)4p\,{}^4D$, respectively. Collectively, these two excitations represent an important indirect mechanism for populating the ^4D term of $3p^4({}^3P)4p$. As will be discussed in section 3, this is due to the large cross section for the second excitation (see figure 4) coupled with a relatively small radiative rate from $3p^4({}^3P)4s\,{}^4P$ to the ground term. Although it is difficult to tell on the scale of figure 3, the extra coupling effects included in the 40-state calculation, as compared with the 28-state calculation, reduce the background cross section for the excitation from the ground term to $3p^4({}^3P)4s\,{}^4P$ by about 30% at 30 eV; however, this difference decreases rapidly with energy. We see from figure 4 that the resonance

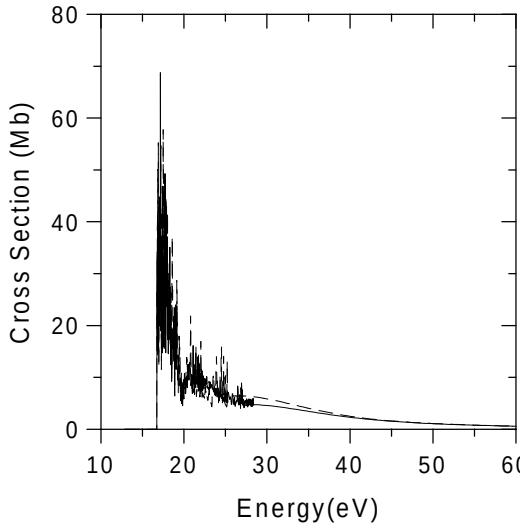

Figure 3. Electron-impact excitation cross section for the transition $3p^5\,{}^2P \rightarrow 3p^4({}^3P)4s\,{}^4P$ in Ar^+ from a 28-state *R*-matrix CC calculation (broken curve) and a 40-state *R*-matrix CC calculation (full curve).

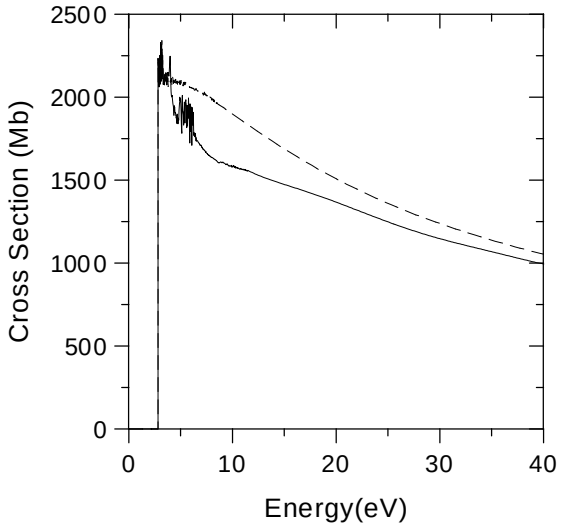

Figure 4. Electron-impact excitation cross section for the transition $3p^4({}^3P)4s\,{}^4P \rightarrow 3p^4({}^3P)4p\,{}^4D$ in Ar^+ from a 28-state *R*-matrix CC calculation (broken curve) and a 40-state *R*-matrix CC calculation (full curve).

contribution to the strong dipole-allowed excitation from $3p^4({}^3P)4s\,{}^4P$ to $3p^4({}^3P)4p\,{}^4D$ is quite small and that the extra coupling effects included in the 40-state calculation reduce the background cross section at the 20% level at 10 eV. One could also introduce pseudostates, that were constructed using e.g. Laguerre orbitals, into the *CC expansion* as opposed to just the CI expansion (Bray and Stelbovics 1993). This would allow for target coupling to highly-excited bound states and to the continuum, within the *R*-matrix calculation (Bartschat *et al* 1996). This could further reduce the background cross section by $\sim 20\%$. However, such a calculation is currently impractical for an ion as complex as Ar^+.

In figures 5 and 6, we compare the 28- and 40-state CC calculations of excitation from the ground term to $3p^4({}^3P)4s\,{}^2P$ and excitation from $3p^4({}^3P)4s\,{}^2P$ to $3p^4({}^3P)4p\,{}^2D$, respectively. Again these excitations provide an indirect path for populating the $3p^4({}^3P)4p\,{}^2D$ term; however, as we shall see, this path is suppressed at lower electron densities by the large radiative rate from $3p^4({}^3P)4s\,{}^2P$ to the ground term (see table 2).

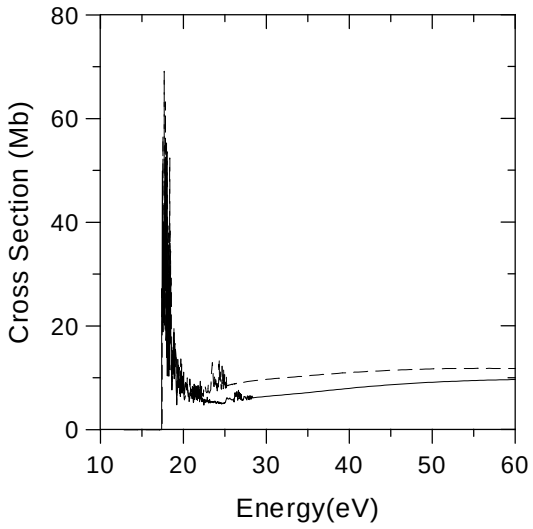

Figure 5. Electron-impact excitation cross section for the transition $3p^5\,^2P \rightarrow 3p^4(^3P)4s\,^2P$ in Ar^+ from a 28-state R-matrix CC calculation (broken curve) and a 40-state R-matrix CC calculation (full curve).

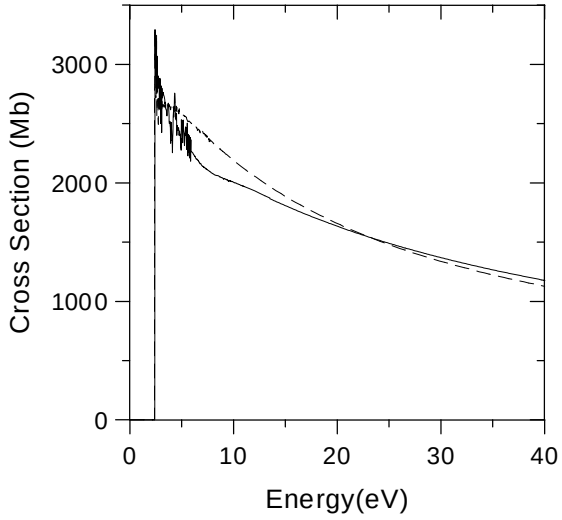

Figure 6. Electron-impact excitation cross section for the transition $3p^4(^3P)4s\,^2P \rightarrow 3p^4(^3P)4p\,^2D$ in Ar^+ from a 28-state R-matrix CC calculation (broken curve) and a 40-state R-matrix CC calculation (full curve).

Here the corrections included within the 43-term CI basis for LS term dependence, as well as the additional coupling effects included in the 40-state CC expansion, account for the differences between the two calculations of the cross sections for these dipole-allowed transitions.

The effective collision strength, Υ, first introduced by Seaton (1953) is defined by the equation

$$\Upsilon_{ij} = \int_0^\infty \Omega(i \rightarrow j) \exp\left(\frac{-\epsilon_j}{kT_e}\right) \mathrm{d}\left(\frac{\epsilon_j}{kT_e}\right), \tag{1}$$

where Ω is the collision strength for the transition from term i to term j and ϵ_j is the continuum energy of the final scattered electron. The effective collision strength is very convenient for interpolation with respect to the electron temperature, T_e, because it has a much more gradual variation with temperature than that of the rate coefficient.

The rate coefficients for collisional excitation, $q_{i\rightarrow j}$, and de-excitation, $q_{j\rightarrow i}$, are then

Table 3. Selected effective collision strengths for Ar^+ from the 40-state (28-state) CC calculation.

	Temperature (eV)							
Transition[a]	0.35	0.69	1.72	3.45	6.89	17.2	34.5	68.9
1–14	0.91	0.97	0.94	0.84	0.69	0.48	0.33	0.22
	(0.89)	(0.96)	(0.93)	(0.84)	(0.71)	(0.50)	(0.35)	(0.24)
1–15	1.08	1.08	1.00	0.86	0.72	0.59	0.51	0.42
	(0.94)	(0.98)	(0.96)	(0.87)	(0.77)	(0.66)	(0.57)	(0.46)
1–4	2.36	2.32	1.94	1.55	1.20	0.80	0.54	0.35
	(2.69)	(2.61)	(2.18)	(1.73)	(1.33)	(0.89)	(0.60)	(0.38)
4–14	65.1	72.2	87.7	108	145	230	322	433
	(65.2)	(73.4)	(93.1)	(119)	(162)	(253)	(341)	(440)
1–6	2.60	2.30	1.69	1.31	1.14	1.46	2.22	3.40
	(2.73)	(2.53)	(1.90)	(1.53)	(1.42)	(1.88)	(2.70)	(3.83)
6–15	39.1	42.5	52.0	64.9	86.9	136	186	242
	(37.8)	(41.7)	(52.6)	(66.7)	(89.9)	(137)	(182)	(232)

[a] The term indices for the transitions are those listed in table 1.

determined from the equations

$$q_{i\to j} = \frac{2\sqrt{\pi}\alpha c a_0^2}{\omega_i}\sqrt{\frac{I_{\mathrm{H}}}{kT_{\mathrm{e}}}}\exp\left(-\frac{\Delta E_{ij}}{kT_{\mathrm{e}}}\right)\Upsilon_{ij}, \tag{2}$$

and

$$q_{j\to i} = \frac{\omega_i}{\omega_j}\exp\left(\frac{\Delta E_{ij}}{kT_{\mathrm{e}}}\right)q_{i\to j}, \tag{3}$$

where $2\sqrt{\pi}\alpha c a_0^2 = 2.1716 \times 10^{-8}$ cm^3 s^{-1}, $I_{\mathrm{H}} = 13.6058$ eV, ΔE_{ij} is the threshold energy for the transition from term i to term j, and ω_i and ω_j are the statistical weights of the initial and final terms, respectively. These rate coefficients are calculated internally in ADAS from the values of the effective collision strengths.

In table 3, we give the effective collision strengths for all transitions shown in figures 1–6. As would be expected from the cross section plots, there are relatively small differences between the effective collision strengths determined from the 28-state CC calculation and those determined from the 40-state CC calculation. This reasonably good agreement between the effective collision strengths from these two R-matrix calculations is found for most other transitions as well. However, the 40-state CC calculation still has the advantage of providing a more complete picture of the effects of higher-lying terms on our collisional–radiative modelling of this system. The calculated values of Υ for all transitions between the 28 terms in the 28-state CC calculation and the first 36 terms from the 40-state CC calculation were entered into the ADAS database for our collisional–radiative calculations for Ar^+.

2.3. Electron-impact ionization

Accurate theoretical calculations of ionization from neutral and near-neutral species remains a difficult problem. Recent progress has been made in incorporating correlation between the scattered and ejected electrons for hydrogen and hydrogen-like targets using a variety of

methods such as the converged CC method (Bray and Stelbovics 1993), the intermediate-energy R-matrix method (Burke *et al* 1987), the R-matrix with pseudostates method (Bartschat *et al* 1996, Bartschat and Bray 1996), and time-dependent methods (Pindzola and Schultz 1996, Pindzola and Robicheaux 1996). The converged CC method and the R-matrix method with pseudostates has also been applied to some simple non-hydrogenic systems; however, none of these methods have been attempted on a species as complex as singly ionized argon.

The DW approximation has been quite successful for the determination of ionization cross sections for highly ionized species, where the effects of correlations are usually not significant. We have developed a DW programme that employs a CA approximation (Pindzola *et al* 1986), as well as a term-to-term DW programme that can incorporate a limited amount of electron correlation (Griffin *et al* 1995). In the case of the CA calculations, it is possible to resolve the cross sections to individual LS terms or LSJ levels using purely algebraic transformations (Sampson 1986), and this is normally the technique we employ to generate ionization data for collisional–radiative modelling calculations (Pindzola *et al* 1995a). However, the discrepancies between experiment and DW theory are often quite significant for complex neutral and near-neutral species, and first-order DW-Born theory, when applied to such systems, can be very sensitive to the scattering potential (Pindzola *et al* 1995b) and bound-state and continuum-electron correlations (Griffin *et al* 1995).

In figure 7, we show a CA DW calculation of the rate coefficient for ionization from the ground term of Ar^+ in comparison with a rate coefficient determined from a fit to the experimental cross section of Müller *et al* (1985). In this calculation, the prior form of the scattering amplitude was employed in which the incident, scattered, and ejected electrons were calculated in the V^{N-1} potential of Ar^{2+}. As can be seen, the theoretical rate coefficient is slightly below the one determined from experiment. This is somewhat surprising since electron correlation normally reduces the first-order DW cross section, as it does in the case of the corresponding atom, neutral Cl (Griffin *et al* 1995). To ensure the most accurate ionization rate possible for the collisonal-radiative (CR) modelling of this problem, we entered the ionization rate determined from the experimental cross section into the ADAS database.

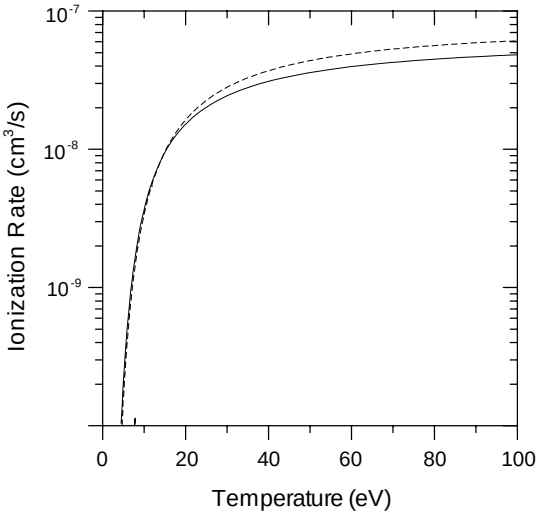

Figure 7. Electron-impact ionization rate coefficient for ionization from the $3p^5\ ^2P$ ground term of Ar^+ from a configuration-average distorted-wave calculation (full curve) and calculated from a fit to the experimental cross section measurements of Müller *et al* (1985) (short-broken curve).

3. Population modelling theory

3.1. Three-state model of impurity influx from only the ground state

A simple three-state model can be used to explain qualitatively many of the basic features in the determination of impurity influx when only the ground term contributes to the ionization of Ar^+. We begin by considering line emission from the $3p^4(^3P)4p\,^4D \rightarrow 3p^4(^3P)4s\,^4P$ transition as our diagnostic example, and therefore limit ourselves to the following three population densities: $N_1(3p^5\,^2P)$, $N_2(3p^4(^3P)4s\,^4P)$, and $N_3(3p^4(^3P)4p\,^4D)$. The CR equations are given by

$$\frac{dN_1}{dt} = C_{11}N_1 + C_{12}N_2 + C_{13}N_3, \tag{4}$$

$$\frac{dN_2}{dt} = C_{21}N_1 + C_{22}N_2 + C_{23}N_3, \tag{5}$$

$$\frac{dN_3}{dt} = C_{31}N_1 + C_{32}N_2 + C_{33}N_3, \tag{6}$$

where C_{ij} are elements of the CR matrix. If we assume that the CR matrix only contains collisional-excitation rates, $N_e q_{i\rightarrow j}$; collisional de-excitation rates, $N_e q_{j\rightarrow i}$; and radiative decay rates, $A_{j\rightarrow i}$; then

$$C_{ii} = -\sum_{j<i} A_{i\rightarrow j} - N_e \sum_{j\neq i} q_{i\rightarrow j}, \tag{7}$$

$$C_{ij} = A_{j\rightarrow i} + N_e q_{j\rightarrow i} \qquad (j > i), \tag{8}$$

$$C_{ij} = N_e q_{j\rightarrow i} \qquad (j < i), \tag{9}$$

where N_e is the electron density. We assume that the population of each of the excited terms is in quasistatic equilibrium with respect to the population of the ground term; therefore, we set $dN_2/dt = dN_3/dt = 0$. The population of the third term is then given by:

$$N_3 = N_e F^{exc}_{1\rightarrow 3} N_1, \tag{10}$$

where

$$N_e F^{exc}_{1\rightarrow 3} = \frac{-C_{22}C_{31} + C_{32}C_{21}}{C_{22}C_{33} - C_{23}C_{32}}. \tag{11}$$

$F^{exc}_{1\rightarrow 3}$ is defined as the effective contribution to the excited population of term 3 via excitation from the ground term 1. Upon substitution from equations (7)–(9) we obtain:

$$\begin{aligned} N_e F^{exc}_{1\rightarrow 3} = {} & [(A_{2\rightarrow 1} + N_e q_{2\rightarrow 1} + N_e q_{2\rightarrow 3})(N_e q_{1\rightarrow 3}) + (N_e q_{2\rightarrow 3})(N_e q_{1\rightarrow 2})] \\ & \times [(A_{2\rightarrow 1} + N_e q_{2\rightarrow 1} + N_e q_{2\rightarrow 3})(A_{3\rightarrow 1} + A_{3\rightarrow 2} + N_e q_{3\rightarrow 1} + N_e q_{3\rightarrow 2}) \\ & -(A_{3\rightarrow 2} + N_e q_{3\rightarrow 2})(N_e q_{2\rightarrow 3})]^{-1}. \end{aligned} \tag{12}$$

If we assume that $A_{2\rightarrow 1}$ is not equal to zero, then in the zero density limit we obtain:

$$F^{exc}_{1\rightarrow 3} = \frac{q_{1\rightarrow 3}}{A_{3\rightarrow 1} + A_{3\rightarrow 2}}. \tag{13}$$

If we consider the situation of atoms emerging from a localized surface and being ionized successively, the total impurity flux, Γ, along a line-of-sight directed at the surface is given by:

$$\Gamma = \int_0^\infty N_e S_1 N_1(x)\, dx, \tag{14}$$

where S_1 is the ionization rate coefficient from the ground term and $N_1(x)$ is the population density of the ground term at position x. If the line-of-sight emissivity is given by:

$$I = \int_0^\infty A_{3\to2} N_3(x)\,\mathrm{d}x, \tag{15}$$

then equation (10) may be used to obtain a direct relation between impurity flux and emissivity:

$$\Gamma = SXB_{1,3\to2} I, \tag{16}$$

where

$$SXB_{1,3\to2} = \frac{S_1}{A_{3\to2} F^{\mathrm{exc}}_{1\to3}}. \tag{17}$$

In the zero-density limit, we obtain:

$$SXB_{1,3\to2} = \frac{S_1}{q_{1\to3} B_{3\to2}}, \tag{18}$$

where

$$B_{3\to2} = \frac{A_{3\to2}}{A_{3\to1} + A_{3\to2}} \tag{19}$$

is the branching ratio for radiative decay from term 3 to term 2.

We carried out three-state model calculations not only for the $3p^4(^3P)4p\,^4D \to 3p^4(^3P)4s\,^4P$ transition in Ar^+, but also for the $3p^4(^3P)4p\,^2D \to 3p^4(^3P)4s\,^2P$ transition. We extracted the necessary effective collision strengths for these calculations from the 40-state *R*-matrix CC calculation. The excitation, de-excitation, and ionization rate coefficients employed, at the three temperatures considered—3.45, 17.2 and 34.5 eV—are given in table 4. Collisional–radiative calculations with ADAS for the ionization balance of Ar indicate that the peak fractional abundance of Ar^+ occurs at about 1.8 eV and has a value greater than 0.1 over 1–3 eV. These findings are virtually independent of the electron density, up to $\sim 10^{15}$ cm^{-3}. However, our SXB ratios are perfectly valid at much higher temperatures, which we show here to better illustrate their variation with temperature.

In figures 8 and 9, we show the SXB ratios for the $3p^4(^3P)4p\,^4D \to 3p^4(^3P)4s\,^4P$ and $3p^4(^3P)4p\,^2D \to 3p^4(^3P)4s\,^2P$ radiative transitions, respectively, as calculated from equation

Table 4. The excitation, de-excitation and ionization rate coefficients employed in the three-state SXB ratio calculations.

T_e (eV)	$q_{1\to2}$ (cm^3 s^{-1})	$q_{2\to1}$ (cm^3 s^{-1})	$q_{1\to3}$ (cm^3 s^{-1})	$q_{3\to1}$ (cm^3 s^{-1})	$q_{2\to3}$ (cm^3 s^{-1})	$q_{3\to2}$ (cm^3 s^{-1})	S_1 (cm^3 s^{-1})
			1. $3p^4(^3P)4p\,^4D \to 3p^4(^3P)4s\,^4P$				
3.45	9.3×10^{-11}	5.9×10^{-9}	2.1×10^{-11}	1.8×10^{-9}	1.7×10^{-7}	2.3×10^{-7}	1.1×10^{-11}
17.2	9.7×10^{-10}	1.3×10^{-9}	5.8×10^{-10}	6.2×10^{-10}	3.1×10^{-7}	2.2×10^{-7}	1.3×10^{-8}
34.5	7.6×10^{-10}	6.2×10^{-10}	4.3×10^{-10}	2.3×10^{-10}	3.4×10^{-7}	2.2×10^{-7}	3.3×10^{-8}
			2. $3p^4(^3P)4p\,^2D \to 3p^4(^3P)4s\,^2P$				
3.45	6.0×10^{-11}	9.3×10^{-9}	2.0×10^{-11}	3.7×10^{-9}	2.4×10^{-7}	9.8×10^{-8}	1.1×10^{-11}
17.2	1.7×10^{-9}	4.7×10^{-9}	6.0×10^{-10}	1.1×10^{-9}	3.8×10^{-7}	2.6×10^{-7}	1.3×10^{-8}
34.5	3.0×10^{-9}	5.0×10^{-9}	6.6×10^{-10}	7.0×10^{-9}	4.0×10^{-7}	2.5×10^{-7}	3.3×10^{-8}

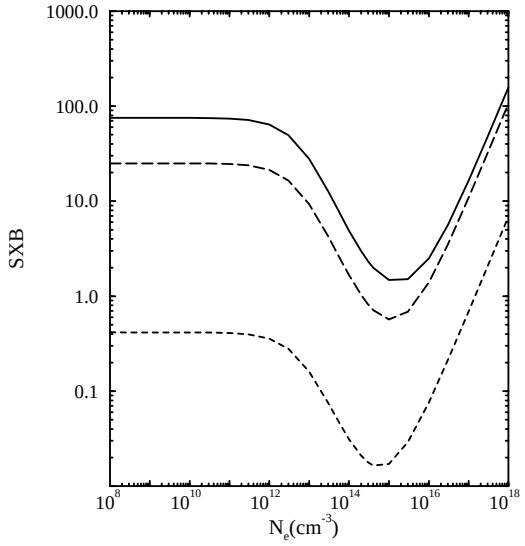

Figure 8. *SXB* ratios as a function of electron density for the radiative transition $3p^4(^3P)4p\,^4D \rightarrow 3p^4(^3P)4s\,^4P$ in Ar^+ from a three-state CR model at electron temperatures of 3.45 eV (short-broken curve), 17.2 eV (long-broken curve), and 34.5 eV (full curve).

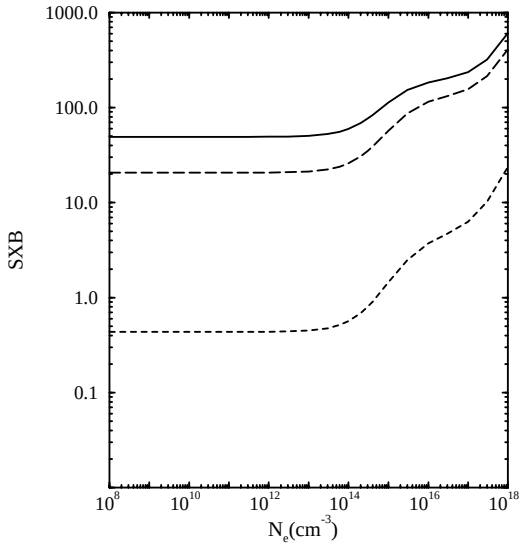

Figure 9. *SXB* ratios as a function of electron density for the radiative transition $3p^4(^3P)4p\,^2D \rightarrow 3p^4(^3P)4s\,^2P$ in Ar^+ from a three-state CR model at electron temperatures of 3.45 eV (short-broken curve), 17.2 eV (long-broken curve), and 34.5 eV (full curve).

(17) at these three temperatures and as a function of electron density. In the zero-density limit, the *SXB* ratios are given by equation (18), while in the high-density limit the product $N_e F^{exc}_{1\rightarrow 3}$ becomes a constant and the *SXB* ratios from equation (17) are a linear function of the electron density.

There are striking differences between these two sets of curves. In the case of the $3p^4(^3P)4p\,^4D \rightarrow 3p^4(^3P)4s\,^4P$ radiative transition, the *SXB* ratio curves drop significantly from their zero-density limiting values beginning at a density of about 10^{12} cm^{-3}, reach a minimum at about 10^{15} cm^{-3}, and then begin to rise in a linear fashion. On the other hand, for the $3p^4(^3P)4p\,^2D \rightarrow 3p^4(^3P)4s\,^2P$ radiative transition, the curves remain equal to their zero-density limiting values until we reach a density of about 10^{14} cm^{-3} and then they begin to rise; however, that increase does not become linear until the density is greater than 10^{17} cm^{-3}.

These pronounced differences can be understood by considering the size of the radiative rate from the second term to the ground term ($A_{2\to1}$) in the three-state models for these two transitions. In the case of the $3p^4(^3P)4p\,^4D \to 3p^4(^3P)4s\,^4P$ radiative transition, the value of ($A_{2\to1}$) from our intermediate coupling calculation is only 5.29×10^6 s^{-1}; this spin-changing radiative rate would be zero except for weak spin–orbit mixing of the levels of $3p^4(^3P)4s\,^4P$ with the levels of $3p^4(^3P)4s\,^2P$, and its value has low reliability. On the other hand, the value of ($A_{2\to1}$) in the three-state model for the $3p^4(^3P)4p\,^2D \to 3p^4(^3P)4s\,^2P$ transition is 2.96×10^9 s^{-1} (see table 2), and its value should be quite reliable.

In the models for both of these transitions, the values of $q_{2\to3}$ are of order 10^{-7} cm^3 s^{-1} (see table 4). Thus, for the quartet radiative transition, the collisional rate from term 2 to term 3 ($N_e q_{2\to3}$) is comparable with $A_{2\to1}$ when the density reaches a value of order 10^{13} cm^{-3}; at such intermediate densities, the indirect process of collisional excitation to term 2 followed by collisional excitation to term 3 will begin to increase the value of $F^{\rm exc}_{1\to3}$ significantly, and thereby lower the SXB ratio. This reduction in the SXB ratio will continue until the density becomes large enough that the terms in equation (12) that are proportional to N_e^2 begin to completely dominate; $N_e F^{\rm exc}_{1\to3}$ will finally approach a constant, at which point the SXB ratio will increase linearly with density.

In the model for the doublet transition this same indirect process for populating term 3 will also contribute; however, since $A_{2\to1}$ is now of order 10^9 s^{-1}, the rate for collisional excitation from term 2 to term 3 ($N_e q_{2\to3}$) will not be comparable with $A_{2\to1}$ until the density is of order 10^{16} cm^{-3}; indeed, it is precisely this process that causes a noticeable decrease in the positive slope of the SXB ratio versus density in figure 9 above 10^{16} cm^{-3}.

We have also investigated the sensitivity of the SXB ratio to the value of the radiative rate from term 2 to term 1 in the three-state model for both types of radiative transitions. In figure 10, we show the SXB ratio corresponding to the quartet radiative transition at an electron temperature of 17.2 eV, as we vary the value of $A_{2\to1}$ from zero (chain curve), to half the calculated value of 5.29×10^6 s^{-1} (short-broken curve), to the calculated value (full curve), and finally to twice the calculated value (long-broken curve). The value of zero was included since the radiative rate from the $3p^4(^3P)4s\,^4P_{5/2}$ level to the levels of the $3p^5\,^2P$ term is zero. In this case, the SXB ratio in the low-density limit differs from that obtained

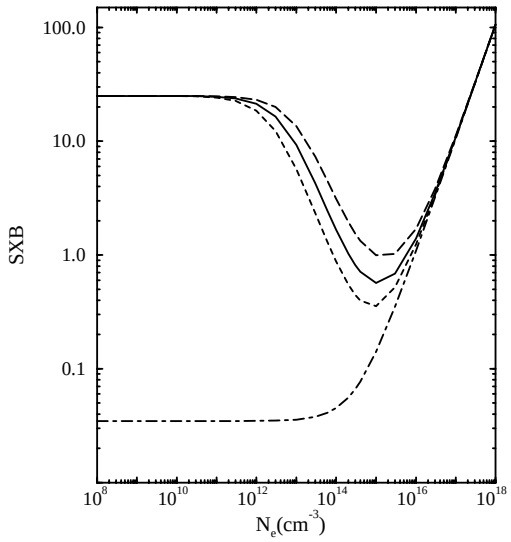

Figure 10. SXB ratios as a function of electron density for the radiative transition $3p^4(^3P)4p\,^4D \to 3p^4(^3P)4s\,^4P$ in Ar^+ from a three-state CR model at an electron temperature of 17.2 eV with $A_{2\to1} = 0.0$ s^{-1} (chain curve): $A_{2\to1} = 2.65\times10^6$ s^{-1} (short-broken curve); $A_{2\to1} = 5.29\times10^6$ s^{-1} (full curve); and $A_{2\to1} = 10.58\times10^6$ s^{-1} (long-broken curve).

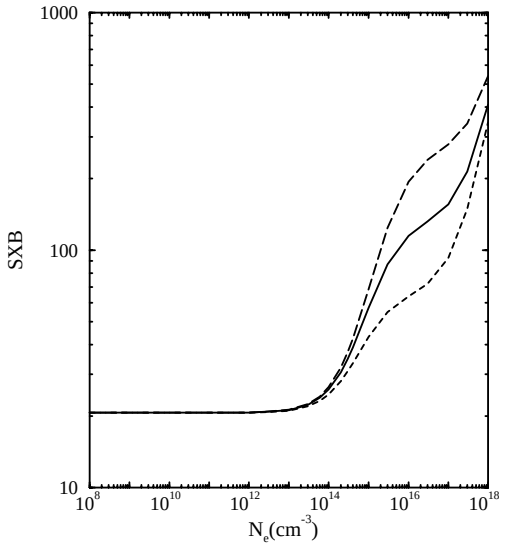

Figure 11. SXB ratios as a function of electron density for the radiative transition $3p^4(^3P)4p\,^2D \rightarrow 3p^4(^3P)4s\,^2P$ in Ar^+ from a three-state CR model at an electron temperature of 17.2 eV with $A_{2\rightarrow1} = 1.48 \times 10^9$ s^{-1} (short-broken curve); $A_{2\rightarrow1} = 2.96 \times 10^9$ s^{-1} (full curve); and $A_{2\rightarrow1} = 5.92 \times 10^9$ s^{-1} (long-broken curve).

from equation (18) by nearly three orders of magnitude. However, even the variation of $A_{2\rightarrow1}$ by a factor 4 causes significant differences in the SXB ratios shown by the short-broken and long-broken curves, and it is doubtful that our calculated value is known to this accuracy since it is so sensitive to very small variations in the intermediate-coupling eigenvectors.

In addition to the uncertainty in the average radiative rate for this transition, its variation with the levels of $3p^4(^3P)4s\,^4P$ is also large. As mentioned above, the radiative rate from $3p^4(^3P)4s\,^4P_{5/2}$ to the levels of the ground term is zero, while the radiative rate from $3p^4(^3P)4s\,^4P_{3/2}$ to the levels of $3p^5\,^2P$ is calculated to be 1.3×10^7 s^{-1} and that from $3p^4(^3P)4s\,^4P_{1/2}$ is found to equal 5.3×10^6 s^{-1}. Even more troubling is the fact that this large variation in the SXB ratio with the value of $A_{2\rightarrow1}$ is most significant in precisely the density range most applicable to a fusion plasma in the divertor region.

In figure 11, we show the SXB ratio corresponding to the doublet radiative transition at an electron temperature of 17.2 eV, as we vary the value of $A_{2\rightarrow1}$ from half the calculated value of 2.96×10^9 s^{-1} (short-broken curve), to the calculated value (full curve), and finally to twice the calculated value (long-broken curve). In this case, the variation in the radiative rate has little effect on the SXB ratio until we reach a density of about 10^{14} cm^{-3}. Although above this density the difference in the SXB ratios becomes large, it is important to keep in mind that our calculated value of $A_{2\rightarrow1}$ should be accurate to much better than a factor of 2 and the variation of the radiative rate to the levels of the ground term from the two levels of $3p^4(^3P)4s\,^2P$ is negligible. Thus, we would expect the accuracy of our calculated SXB ratio to be better for the doublet transition than for the quartet transition.

3.2. Many-state calculations of impurity influx from only the ground state

Next, we again assumed that only the ground term contributes to the ionization of Ar^+, but carried out full CR calculations for the SXB ratios for the same two optical transitions in Ar^+ discussed above, using the effective collision strengths from both our 28- and 40-state R-matrix CC calculations. We first performed calculations in which only the first 22 terms listed in table 1 were included in the CR model and rates from both the 28- and 40-state CC

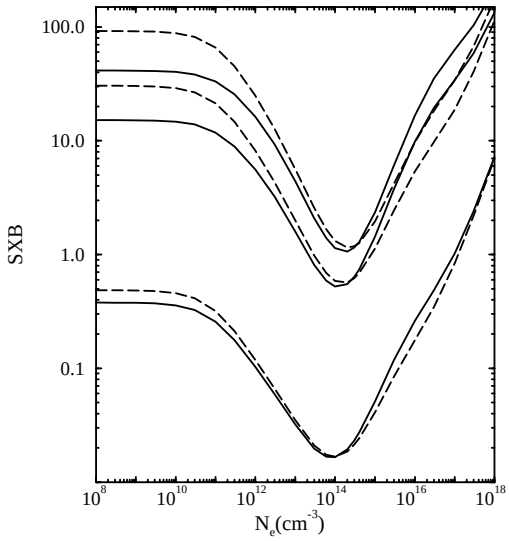

Figure 12. SXB ratios as a function of electron density for the radiative transition $3p^4(^3P)4p\,^4D \rightarrow 3p^4(^3P)4s\,^4P$ in Ar^+ from a 22-state CR model (broken curves) and a 36-state CR model (full curves) at electron temperatures of 3.45, 17.2 and 34.5 eV.

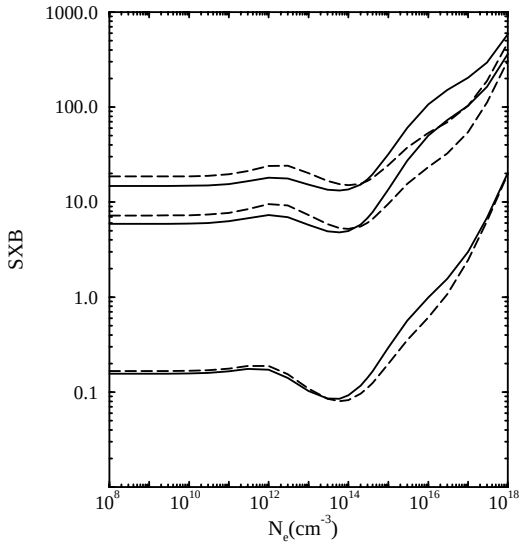

Figure 13. SXB ratios as a function of electron density for the radiative transition $3p^4(^3P)4p\,^2D \rightarrow 3p^4(^3P)4s\,^2P$ in Ar^+ from a 22-state CR model (broken curves) and a 36-state CR model (full curves) at electron temperatures of 3.45, 17.2 and 34.5 eV.

calculations were employed. The first 22 terms were selected since the energies resulting from the two CI calculations are in good agreement up to that point (see table 1). As we might expect, the variation of the SXB ratios with these two sets of collisional-excitation data for both radiative transitions was quite small.

We then investigated the variation of these SXB ratios with the number of terms included in the CR modelling. In figures 12 and 13, we show our results for the quartet and doublet radiative transitions, respectively, at the same three temperatures (3.45, 17.2 and 34.5 eV) used in the three-state calculations when the lowest 22 terms from the 40-state CC calculation are included (long-broken curves) and when the lowest 36 terms from the 40-state CC calculation are included (full curves). We see that the differences between these calculations are more pronounced in the case of the quartet transition. We also note that in figure 12 the SXB ratios begin to decrease at a lower density and do so more

gradually than in the case of the three-state model calculations for this same transition in figure 8. On the other hand, the differences with respect to shape between the three-state model shown in figure 9 and these more complete CR models for the doublet transitions are less pronounced. However, the intermediate-density SXB ratios are no longer completely independent of density, as they were in the simple three-state model.

The more gradual decline in the SXB ratios for the quartet transition in the 22- and 36-state modelling calculations appears to be due to the effect of excitation to the quartet metastable terms of $3p^4 3d$ ($q_{1\rightarrow 3,5,8}$) followed by excitation from these metastable terms to $3p^4(^3P)4p\,^4D$. These indirect processes will increase the effective contribution to the excited population, $F^{\rm exc}_{1\rightarrow 14}$, where N_{14} is the population of $3p^4(^3P)4p\,^4D$, since these metastable terms have small radiative rates to the ground term and relatively large collisional-excitation rates to $3p^4(^3P)4p\,^4D$. This was confirmed by repeating the 36-state modelling calculation with all of the collisional rates from these quartet metastable terms to $3p^4(^3P)4p\,^4D$ set to zero. The shape of the resulting curve of the SXB ratio as a function of density was much more like that of the three-state model shown in figure 8.

There are small dips which appear in the SXB ratio curves in the more complete CR models shown in figure 13, for the doublet transition just below a density of 10^{14} cm^{-3}, that do not appear in the three-state model curves shown in figure 9. These are primarily due to the indirect process of excitation to the $3p^4(^3P)3d\,^2F$ term ($q_{1\rightarrow 10}$) followed by excitation to $3p^4(^3P)4p\,^2D$ ($q_{10\rightarrow 15}$). The values of $q_{10\rightarrow 15}$ are of order 10^{-7} cm^3 s^{-1} while the radiative rate from $3p^4(^3P)3d\,^2F$ to the ground term ($A_{10\rightarrow 1}$) is calculated to be 2.38×10^6 s^{-1}. Thus, at a density of about 10^{13} cm^{-3}, the value of $N_e q_{10\rightarrow 15}$ will begin to increase the effective contribution to the excited population, $F^{\rm exc}_{1\rightarrow 15}$, where N_{15} is the population of $3p^4(^3P)4p\,^2D$, and thereby decrease the SXB ratio.

In the case of both the doublet and quartet transitions, the low-density limits are quite different when more states are included in the CR modelling. For example, at a temperature of 34.5 eV, the low-density SXB ratio for the quartet transition from the three-state model is 75.3, while in the case of the 36-state model it is equal to 41.4. For the doublet transition at the same temperature, the low-density SXB ratio is 49.3 from the three-state model, but decreases to a value of 14.8 when we apply the 36-state model. The reduction in these SXB ratios is primarily due to radiative cascades from higher terms; however, in the case of the quartet transition, the decrease in the SXB ratio due to cascades is partially off-set by an increase in the SXB ratio due to radiative branching to lower terms (see equation (18)).

We have analysed these cascades in some detail for the case of the doublet transition. The effective contribution to the excited population, $F^{\rm exc}_{1\rightarrow 15}$, is strongly enhanced by cascade from certain higher-lying terms, resulting in a much smaller SXB ratio than that predicted by the three-state model. The main cascade contribution comes from the $3p^5\,^2P \rightarrow 3p^4(^1D)3d\,^2F$ collisional excitation ($q_{1\rightarrow 19}$) followed by radiative decay to the $3p^4(^3P)4p\,^2D$ term ($A_{19\rightarrow 15}$). The cascade contribution generally involves the weaker excitation transitions. Although the strongest ground-term excitation for Ar^+ is the $3p^5\,^2P \rightarrow 3p^4(^3P)3d\,^2D$ transition ($q_{1\rightarrow 27}$), it contributes almost nothing to cascade because the reverse radiative transition ($A_{27\rightarrow 1}$) is also very strong.

We have supported this explanation of the cascade contribution to the doublet transition by performing a four-state modelling calculation which included only the $3p^5\,^2P$, $3p^4(^3P)4s\,^2P$, $3p^4(^3P)4p\,^2D$, and $3p^4(^1D)3d\,^2F$ terms. The value of the SXB ratio from this calculation was 19.5, indicating that the most important cascade originates with the $3p^4(^1D)3d\,^2F$ term. A portion of the remaining reduction in the SXB ratio seems to come from the $3p^4(^1D)4p\,^2F$ and $3p^4(^1D)4p\,^2D$ terms radiatively cascading to $3p^4(^1D)3d\,^2F$. This

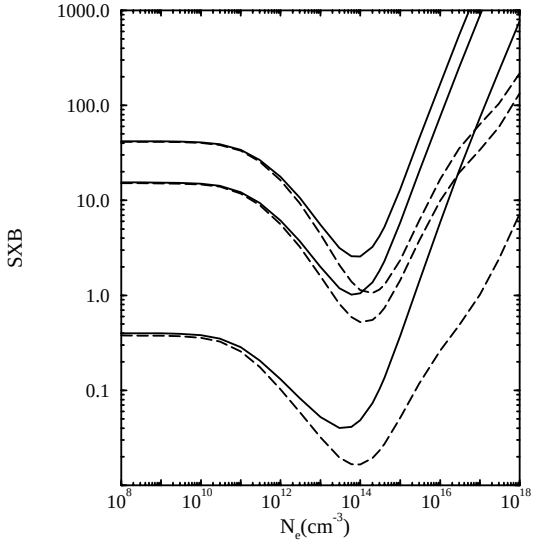

Figure 14. *SXB* ratios as a function of electron density for the radiative transition $3p^4(^3P)4p\,^4D \rightarrow 3p^4(^3P)4\,^4P$ in Ar^+ from a 36-state CR model without ionization out of the excited states (broken curves) and with ionization out of the excited states (full curves) at electron temperatures of 3.45, 17.2 and 34.5 eV.

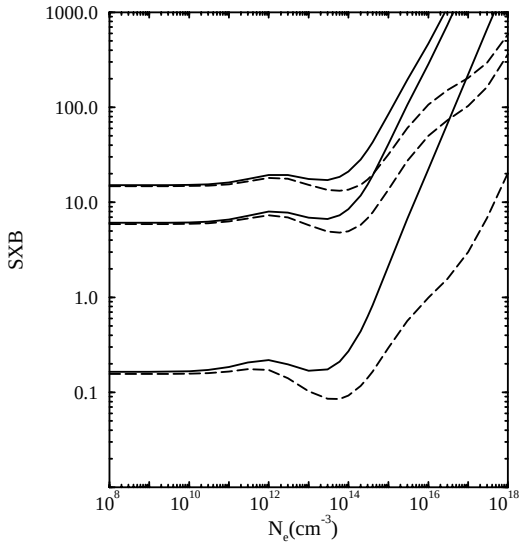

Figure 15. *SXB* ratios as a function of electron density for the radiative transition $3p^4(^3P)4p\,^2D \rightarrow 3p^4(^3P)4s\,^2P$ in Ar^+ from a 36-state CR model without ionization out of the excited states (broken curves) and with ionization out of the excited states (full curves) at electron temperatures of 3.45, 17.2 and 34.5 eV.

was confirmed by performing a six-state modelling calculation which included these two additional terms. Finally, we get additional reduction in this *SXB* ratio through excitation from the ground term to $3p^4(^3P)4d\,^2F$ ($q_{1\rightarrow 30}$), followed by emission from $3p^4(^3P)4d\,^2F$ to $3p^4(^3P)4p\,^2D$ ($A_{30\rightarrow 15}$).

We have repeated the 36-state CR calculations for both the quartet and doublet transitions with the inclusion of ionization out of the excited terms. The rate coefficients for this additional collisional process were generated internally in ADAS from the exchange classical impact parameter method (Burgess and Percival 1968). We present our results with and without excited-state ionization in figures 14 and 15 for the quartet and doublet transitions, respectively. As one would expect, this process has little effect on the *SXB* ratios at lower densities, but increases the *SXB* ratios by a large amount at higher densities. It is interesting to note that the *SXB* ratio for the doublet transition becomes a linear function of density

at much lower densities when ionization out of excited states is included. In figure 15, the full curves represent the recommended SXB data, and the more comprehensive data for this transition are now available in the ADAS database.

3.3. Power loss

Finally, in order to demonstrate the importance of accurate atomic data in the modelling of plasma cooling of Ar^+, we have also carried out calculations of the radiated power loss (coefficient) from Ar^+ using our atomic structure and collisional-excitation data and compared the results with those generated from Born calculations of the excitation rates. The total zero-density line power-loss coefficient for excitation from the ground state is given by

$$P^z_{\mathrm{L},1} = \sum_j \Delta E_{j1} q_{1\to j}, \tag{20}$$

where ΔE_{j1} is the energy of the excitation transition from the ground state to the upper state j. This power-loss coefficient is often parametrized for use in plasma modelling by grouping together the transitions into, for example, four representative ones each with an average transition energy and rate. The parametrized data are chosen so as to match the original data at a single temperature, normally at peak abundance.

A more sophisticated approach to the power-loss coefficient results from CR modelling. The line power-loss coefficient associated with the ground state or a metastable state i is given by

$$P_{\mathrm{L},i} = \sum_{j,k} \Delta E_{jk} A_{j\to k} F^{\mathrm{exc}}_{i\to j}, \tag{21}$$

where ΔE_{jk} is the transition energy for the $j \to k$ radiative transition. The previous zero-density expression (equation (20)) and subsequent results are recovered by solving the CR population rate equations at a suitably low density. Numerical data resulting from equation (21) are used in more accurate modelling.

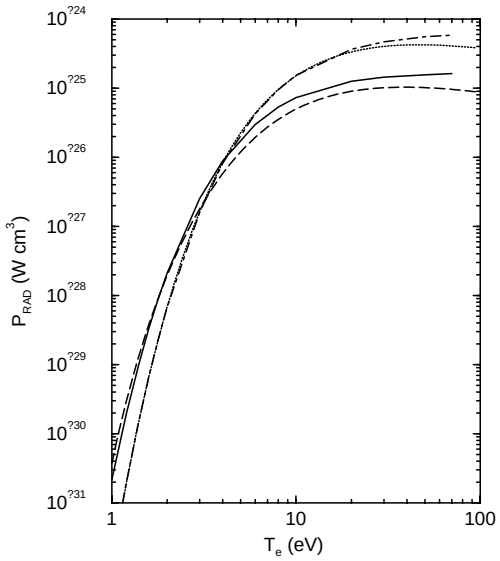

Figure 16. Zero-density line power-loss coefficient for Ar^+ as a function of electron temperature calculated from 'Born' data (chain curve); parametrized 'Born' data (dotted curve); present 43-state CC data (full curve); and parametrized 43-state CC data (broken curve).

In figure 16, we present results for the total zero-density line power-loss coefficient for Ar^+ over 1–100 eV, which covers the temperature range of peak abundance (1–3 eV). Parametrized data are compared with the original data for both the atomic data presented in this paper as well as for that used by ADAS as a default and labelled 'Born'. These latter data are from plane-wave Born calculations of collisional excitation and are generated automatically for the complete isonuclear sequence of an element using a development of Cowan's programme (Cowan 1981); these are the lowest-quality collisional data that are used by ADAS for this purpose. They provide the required energy levels, radiative rates, and Born collisional-excitation rates in a form automatically accessible by ADAS. Level bundling to produce term-resolved data is also handled automatically.

At $\sim$2 eV, the temperature of peak equilibrium fractional abundance of Ar^+ for electron densities up to 10^{15} cm^{-3}, we see that the 'Born' data underestimate the power-loss coefficient by a factor of 3. This is not surprising given the sensitivity of the collision strengths to distortion, coupling effects, and resonant contributions. We see that the parametrization works well for the 'Born' data, only starting to diverge at very high temperatures. The parametrization of our new data does not work quite so well but it is satisfactory in the temperature range where Ar^+ is most abundant. We note that the bulk of the radiated power for argon in the divertor occurs from higher charge states, i.e. at higher temperatures. Finally, parametrized data following equation (20) and numerical data following equation (21) for Ar^+ are now available in the ADAS database together with the related spectral line emissivity data.

4. Summary

We have carried out extensive theoretical calculations of atomic structure, radiative decay, electron-impact excitation, and electron-impact ionization in order to generate the data necessary to model Ar^+ in a plasma environment. Using these data, we have performed a series of CR calculations of SXB ratios in which we assumed that only the ground term contributes to the ionization of Ar^+. We have analysed the SXB ratios associated with a radiative transition between two quartet terms and a second transition between two doublet terms. We have also calculated the zero-density line power-loss coefficient using our collisional-excitation data and compared our results with the power-loss coefficient determined from plane-wave Born excitation data.

Using a simple three-state CR model, we first found that the indirect process of excitation to the intermediate term followed by further sequential excitation to the upper term has a significant effect on the SXB ratio for the quartet transition in the intermediate density regime. The effect of this process on the doublet transition does not occur until we reach higher densities. Furthermore, we discovered that uncertainties in the radiative rate from the intermediate term to the ground term can have large effects on the SXB ratios, especially for the quartet radiative transition. These same effects are found again in a full many-state calculation of the SXB ratios, complicated by the presence of many more intermediate-term pathways. In addition, the process of radiative cascade from terms higher in energy than the upper terms involved in the radiative transition was found to have a pronounced effect on the SXB ratios for both types of transitions. Finally, we discovered that the zero-density line power-loss coefficient for Ar^+ is increased by a factor of 3, at the peak abundance of this ion, when one employs the present collisional-excitation data rather than plane-wave Born collisional-excitation data.

The results of our modelling calculations of the SXB ratios certainly provide insight into the types of CR processes most important to impurity influx in the divertor of a tokamak

reactor. However, additional modelling studies, using the data generated here, may be necessary in order to provide an accurate determination of the influx of argon in such a reactor. For example, ionization out of metastable terms, as well as ionization out of the ground term, may contribute to the total ionization of Ar^+. In order to treat this possibility within our CR modelling calculations, we would no longer assume that the populations of the metastable terms are in quasistatic equilibrium with the population of the ground term. This would eliminate the dependence of our results on the populations of the long-lived states. However, there are significant practical problems associated with this approach. There are as many as seven terms in Ar^+ that could be considered metastable. In order to determine the influx of argon, one must produce SXB ratios corresponding to a set of radiative transitions equal in number to the number of metastable terms plus the ground term (see Badnell *et al* 1996). This would require eight radiative transitions. One would have to calculate theoretical values for the effective contributions to the excited populations ($F^{\mathrm{exc}}_{i\rightarrow j}$) for all eight upper terms in the radiative transitions via excitation from the ground term and all seven metastable terms. Of course, this treatment would also require electron-impact ionization rates from the ground term and each of the seven metastable terms. These data could all be produced from a combination of our theoretical calculations and the use of ADAS. However, it seems impractical to require the measurement of the emissivities for eight optical transitions, in conjunction with these theoretical calculations, in order to determine the total influx of argon.

A more reasonable approach might be to bundle those metastable terms not involved in the optical transitions by spin and produce total rates to, and average rates from, each of these bundled metastable terms. In this case, it would then be possible to reduce the number of required radiative transitions to four. The actual transitions to be used should be determined in collaboration with on-going experimental efforts. However, possible candidates are: $3p^4(^3P)4p\,^4P \rightarrow 3p^4(^3P)4s\,^4P$ and $3p^4(^3P)4p\,^2P \rightarrow 3p^4(^3P)4s\,^2P$, in addition to the two radiative transitions $3p^4(^3P)4p\,^4D \rightarrow 3p^4(^3P)4s\,^4P$ and $3p^4(^3P)4p\,^2D \rightarrow 3p^4(^3P)4s\,^2P$, already considered in this study. One would then treat the $3p^4(^3P)3d\,^4D$, ^4F, and ^4P terms as one bundled quartet metastable term, and the metastable terms $3p^4(^3P)3d\,^2F$ and ^2G as a second bundled doublet metastable term. Ionization out of the $3p^5\,^2P$ ground term, the $3p^4(^3P)4s\,^4P$ metastable term, the bundled quartet metastable term, and the bundled doublet metastable term would then be included in the CR modelling of the impurity influx.

Acknowledgments

This work was supported in part by the US Department of Energy under grant no DE-FG02-96-ER54367 with Rollins College and grant no DE-FG05-96-ER54348 with Auburn University, and by the JET Joint Undertaking and a NATO travel grant CRG 940134 with the University of Strathclyde.

References

Badnell N R, Gorczyca T W, Pindzola M S and Summers H P 1996 *J. Phys. B: At. Mol. Opt. Phys.* **29** 3683
Bartschat K and Bray I 1996 *J. Phys. B: At. Mol. Opt. Phys.* **29** L577
Bartschat K, Hudson E T, Scott M P, Burke P G and Burke V M 1996 *J. Phys. B: At. Mol. Opt. Phys.* **29** 115
Behringer K, Summers H P, Denne B, Forrest M and Stamp M 1989 *Plasma Phys. Control Fusion* **31** 2059
Berrington K A, Eissner W B and Norrington P H 1995 *Comput. Phys. Commun.* **92** 290
Bray I and Stelbovics A T 1993 *Phys. Rev. Lett.* **70** 746
Burgess A 1974 *J. Phys. B: At. Mol. Phys.* **7** L364
Burgess A, Hummer D G and Tully J A 1970 *Phil. Trans. R. Soc.* **266** 225

Burgess A and Percival I C 1968 *Adv. At. Mol. Phys.* **4** 109
Burke P G, Noble C J and Scott M P 1987 *Proc. R. Soc.* **410** 289
Burke V M, Burke P G and Scott N S 1992 *Comput. Phys. Commun.* **69** 76
Cowan R D 1981 *The Theory of Atomic Structure and Spectra* (Berkeley, CA: University of California Press)
Froese Fischer C 1991 *Comput. Phys. Commun.* **64** 369
Gorczyca T W, Robicheaux F, Pindzola M S, Griffin D C and Badnell N R 1995 *Phys. Rev.* A **52** 3877
Griffin D C, Pindzola M S, Gorczyca T W and Badnell N R 1995 *Phys. Rev.* A **51** 2265
Horton L 1996 Private communications
McCracken G 1996 Private communications
Moore C E 1949 *Atomic Energy Levels* NSRDS-NBS no 35 vol I (Washington, DC: US Govt Printing Office)
Müller A *et al* 1985 *J. Phys. B: At. Mol. Phys.* **18** 2993
Pindzola M S, Griffin D C, Badnell N R and Summers H P 1995a *Nucl. Fusion Suppl.* **6** 117
Pindzola M S, Griffin D C and Bottcher C 1986 *NATO ASI Series* B **145** 75
Pindzola M S, Griffin D C and Majek J H 1995b *Phys. Rev.* A **51** 2186
Pindzola M S and Robicheaux F 1996 *Phys. Rev.* A **54** 2142
Pindzola M S and Schultz D R 1996 *Phys. Rev.* A **53** 1
Sampson D H 1986 *Phys. Rev.* A **34** 986
Seaton M J 1953 *Proc. R. Soc.* A **231** 400
Summers H P 1994 Atomic data and analysis structure user manual *JET Joint Undertaking Report* H JET-IR(94)06
Summers H P and Hooper M B 1983 *Plasma Phys.* **25** 1311
Tayal S S and Henry R J W 1996 *J. Phys. B: At. Mol. Opt. Phys.* **29** 3443
Vujnović V and Wiese W L 1992 *J. Phys. Chem.* **21** 919